CrossMark
click for updates

Volume 1 | Number 1 | Jan 2013 | Pages 1–100

PCCP

Physical Chemistry Chemical Physics
www.rsc.org/pccp

ROYAL SOCIETY OF CHEMISTRY

ROYAL SOCIETY OF CHEMISTRY

Journal Name

ARTICLE

Defect structure and optical phonon confinement in ultrananocrystalline Bi$_x$Sn$_{1-x}$O$_2$ (*x* = 0, 0.03, 0.05, 0.08) synthesized by sonochemical method

L. Aswaghosh,[a] DivinahManoharan[b]* and N. VictorJaya[a]

In the present work, the structure of defect and the oxygen vacancy induced optical phonon confinement effect in phase pure tetragonal rutile crystal structured ultrananocrystalline Bi$_x$Sn$_{1-x}$O$_2$ (*x* = 0, 0.03, 0.05, 0.08) with high surface area synthesized by sonochemical method is being reported. As the Bi ion incorporates into the SnO$_2$ host lattice, it replaces the Sn ions marked by the lattice expansion, which leads to the formation of oxygen vacancy so as to maintain charge neutrality. The grain size reduces from 6 nm to 3 nm with increase in Bi content from 0 to 8%. The size effect and the increased oxygen vacancy concentration were found to induce phonon confinement within the grain. This has led to interesting changes in the vibrational spectra of the ultrananocrystalline Bi$_x$Sn$_{1-x}$O$_2$ as the size reduces below 9 nm. Absence of periodicity beyond this critical particle size relaxes the zone-centre optical phonon selection rule, causing the Raman spectrum to have contributions also from phonons away from the Brillouin-zone centre. The structure of defect such as the in-plane, bridging and sub-bridging oxygen vacancy present was confirmed using Raman spectroscopic analysis. The reason for enhancement in PL behaviour with increased Bi content is being discussed. The energy band gap was found to be wider (~4 eV) compared to the bulk and reveals an increasing trend as a function of Bi%. The increase in band gap with decrease in particle size marks the quantum confinement effect. The variation of band gap upon doping is due to the BM shift effect which arises as a result of increase in carrier concentration.

Introduction

Tin (IV) oxide (SnO$_2$) is considered as one of the technologically important material due to its high degree of transparency in the visible region of the electromagnetic spectrum, wide direct band gap (3.6 eV), strong physical and chemical interaction with adsorbed species, n-type semiconducting property, catalytic property and chemical stability.[1-5] SnO$_2$ have gained interest among material researchers in the past decade as it has been used in a wide range of applications namely solar cells, gas sensors, liquid crystal displays, optoelectronic devices, transistors, electrodes for lithium ion batteries, etc.[6-11] Among these numerous applications, developing chemical sensors is an active field of research as it can be used to detect the combustible gases such as H$_2$S, CO, H$_2$, liquid petroleum, toluene, NO, NO$_2$ and C$_2$H$_5$OH.[7, 12-18] It is well-known that the nanomaterials show distinct characteristics superior to their bulk counterparts. Due to the high surface to volume ratio of tin oxide nanoparticles, they are very much suitable for gas sensing applications with increased sensitivity and adsorption. The critical factor to optimize sensor behavior of SnO$_2$-based materials is by the stringent control of both the material grain size and the tin/oxygen stoichiometry. Grain size has been shown to influence both conductivity and sensor sensitivity with optimal sensor performance obtained when the grain diameter approaches the dimension of the charge depletion layer, ≈6 nm.[19] Therefore, it is of great interest to synthesize ultrananocrystalline tin oxide.

The optoelectronic properties such as photoluminescence and optical band gap of SnO$_2$ can be improved by impurity doping. There are several reports on the effect of dopants (Sb, Mn, Co, Fe, Cu, Ni, Ce) on the properties of SnO$_2$.[20–25] It is well known that Bi and Sb have similar chemical properties owing to their similar location in the periodic table of elements. There are various reports on the effect of antimony dopant on the characteristics of SnO$_2$ nanoparticles whereas only limited research has been directed towards SnO$_2$ with bismuth as a dopant. Hitherto, the influence of Bi dopant on SnO$_2$ characteristics is seldom reported. Moreover, Bi is a non-toxic alternative to Sb. Therefore, it is of special interest to study the influence of Bi dopant on structural, optical and electronic properties of SnO$_2$ nanoparticles. Most recently, Bi doped SnO$_2$ has been reported to improve the sensitivity in ethanol vapour sensing application and can be used as acid-resistant anode material in electrochemistry.[18, 26] Bi doped SnO$_2$ coated CNT has been reported to improve anode stability and efficiency in flow through organic electrooxidation.[27]

a. Dept. of Physics,Anna University, Chennai, India.
b. Dept. of Physics, Tamkang University, Taiwan.

In materials science as well as applied research point of view, the preparation and elucidation of related properties of nanocrystalline materials is gaining popularity among the scientific community because of the fact that the material properties change drastically as particle size reduces to nanoscale. It is important to analyze the structural and optoelectronic properties of nanocrystalline semiconductors so as to bring into spotlight the enhanced properties of nanomaterials, thereby enabling them for practical applications. If the particle size of a semiconductor becomes comparable to the Bohr radius of the exciton, so-called quantum size effects occur and the ratio of surface atoms to those in the interior increases remarkably, leading to the surface properties playing an important role in the properties of the material.[28] As a result of these quantum size effects, the band gap of the semiconductor increases, and at the edges of the valence and conduction band discrete energy levels occur.[28] These quantum size effects have stimulated great interest among material scientist as these materials find new applications as devices.

Below a critical size, the optical phonon confinement occurs in the nanostructured material. The critical size is determined by the marked difference in property compared to the bulk. The critical size depends on the method of synthesis due to the defect structures formed and their concentration.[28] Such an optical phonon confinement effect is reported in nanocrystalline ZnO using Raman spectroscopic investigations.[30] Theoretical models and calculations propose that the optical phonon confinement is the reason for asymmetric broadening and the optical phonon Raman line shift, the magnitude of which depends on the widths of the corresponding phonon dispersion curves. Raman techniques could detect only the optical phonons close to the zone centre ($k = 0$). This $k = 0$ selection rule is basically concerned on the infinite periodicity of the crystal lattice.[31, 32] Suppose if the periodicity of the crystal is interrupted, as in the case of nanocrystalline materials, this rule is relaxed. This is owing to the fact that the phonon propagation gets interrupted by the grain boundary in a polycrystalline material. In an isolated grain, the phonon remains confined within the crystal as it is reflected back from the boundaries. The phonon confinement effect is noticeable in the vibrational spectra only when the grain size is smaller than typically 20 lattice parameters.[31] Optical as well as acoustical phonons gets confined within the particle. The highest degree of confinement (3D) occurs in quantum dots and nanoparticles, where the propagation is restricted in all three directions as the dimensionality of the system is zero.

In perfect crystals, only the zone-centre optical phonons can be observed using optical techniques such as Raman spectroscopy. However, the $k = 0$ selection rule is relaxed as a significance of interruption of lattice periodicity in nanocrystalline material. In analogy with electron confinement, phonon confinement has also been found to give rise to interesting changes in the vibrational spectra. The changes in the Raman spectral parameters are expected to be larger as the dimensionality of the system reduces below the

critical size. The presence of zone-boundary phonons in crystals with high defect concentration and in mixed crystals has been reported.[33, 34] This arises because of the relaxation of the $k = 0$ selection rule due to the presence of disorder in the crystal. There are numerous reports on the presence of surface phonons in the Raman spectra of nanostructured materials in addition to the confined optical phonons.[35, 36] Surface phonons are expected to have wavenumbers between TO and LO phonons.[37] Since the fraction of surface atoms increases as the crystallite size of a nanostructured material reduces, surface phonons are observed with noticeable intensity for ultrasmall-size particles. In the present paper, the occurrence of surface phonon band and oxygen vacancy defect induced optical phonon confinement effect as a consequence of ultrasmall size of the bismuth doped tin oxide system is reported.

Both physical and chemical methods have been adapted for the preparation of tin oxide nanoparticles. Chemical methods offer the advantage of being inexpensive and ease of process. Inexpensive methods to synthesize nanoparticles at low temperatures without the need of any special atmosphere are considered the most important objective in synthesis of high quality ultrafine nanoparticles. Methods of tin oxide synthesis include solid state synthesis, microemulsion, sol–gel, gel combustion technique, hydrothermal synthesis and precipitation processes.[38-43] Among these various reported method, precipitation method is used widely owing to the advantages of inexpensive raw materials and short processing times. Co-precipitation is a suitable chemical method for nanoparticles synthesis as it does not require high pressure and temperature and by-products can be eliminated by filtration and washing. However, the particle size cannot be controlled effectively and therefore the precipitation method requires either a physical or chemical aid to control the particle size. In the present work, ultrasonic wave irradiation is used as a physical aid to control the particle size in the oxalate precipitation method.

Materials and Methods

Starting materials

All the chemicals and reagents used were analytical grade and used as such without any further purification. Tin (IV) Chloride pentahydrate ($SnCl_4.5H_2O$) (Sigma-Aldrich), Bismuth (III) nitrate pentahydrate ($Bi(NO_3)_3.5H_2O$) (Sigma-Aldrich), Oxalic acid dihydrate (Merck), 32% extrapure ammonia solution (Merck), Ethanol (Merck) and double distilled water were used for the synthesis.

Sonochemical synthesis of ultrananocrystalline $Bi_xSn_{1-x}O_2$ ($x = 0$, 0.03, 0.05, 0.08)

40 ml of 0.2 M precursor solution in the ratio Sn:Bi::1-x:x (where $x = 0$, 0.03, 0.05 & 0.08) was made by dissolving the precursor salts in double distilled water by stirring. 20 ml of 0.2 M oxalic acid was added drop-wise to the above mixed solution under vigorous stirring. The pH of the solution was adjusted by drop-wise addition of liquid ammonia. The pH of

the final precipitate was maintained at 9. The experimental parameters for the sonochemical reaction were 40 W/cm2 power, 30 min irradiation time and room temperature. The Titanium horn was kept well immersed into precursor solution taken in a round bottom flask in order to facilitate uniform acoustic wave propagation in the reaction mixture. Ultrasonic waves were applied to the primary precursor complex solution to intensify the formation of tin dioxide nuclei and subsequent control over the nuclei growth.[44] The supernatant water was decanted. The precipitate was centrifuged and washed with water and ethanol several times. Then the precipitate was dried in hot air oven at 120°C for 24 hr. The powder was ground using agate mortar and pestle. Then the powders were calcined at 500°C for 2 h in an alumina crucible using a high temperature furnace.

Characterization of the prepared ultrananocrystalline $Bi_xSn_{1-x}O_2$ (x = 0, 0.03, 0.05, 0.08)

The identification of phases in the synthesized ultrananocrystalline powder sample was carried out by X-ray powder diffraction studies at room temperature on a PANanalytical X'pert PRO X-ray diffractometer using Cu Kα radiation (1.54 Å), and comparing the interplanar distances and intensity values with those of the corresponding standard peaks using JCPDS files. All the peaks in the XRD pattern have been indexed to their respective (hkl) planes. The crystallite size of the nanoparticles have been evaluated from X-ray powder diffraction data using Scherrer formula[45] given in equation (1)

$$D = k\lambda/\beta\cos\vartheta \qquad (1)$$

where D is the crystallite size; k = 0.89, a correction factor to account for particle shape; β is the full width at half maximum (FWHM) of the most intense diffraction plane; k is the wavelength of Cu target = 1.54 Å; and ϑ is the Bragg angle. Rietveld powder structure refinement method by using PANanalytical X'Pert High Score Plus software was utilized to determine the microstructural parameters of the synthesized powders (See Supporting information S1). The starting micro-structural parameters of the phases were taken from the database of the Rietveld software.

FE-SEM images were recorded using JEOL 6500 instrument. The TEM images were recorded using JEOL JEM -2100F. Due to the smaller size of the particles and agglomeration, sample preparation for TEM is crucially important. The nanoparticles were dispersed in hexane and coated on a carbon grid. The particle size histogram was obtained by analyzing via random sampling technique using Digital microscope software. The visible Raman spectroscopy was done in Jobin Yvon Lab Raman HR 800 with laser source of wavelength 632.8 nm. The energy band gap was determined from UV-visible spectroscopic data using Tauc plot. Tauc plot is plotted with the nth power of product of absorbance co-efficient (α) and photonic energy (hv) against the electronic energy band gap (E_g). Since tin oxide is considered as a direct band gap semiconductor, the value of n is taken as 2 for allowed transitions. The energy band gap is found out by extrapolating the linear portion of the graph to

the X-axis. As the particle radius goes below the Bohr radius, r_B (2.7 nm for SnO_2), the electron hole motion is not correlated. In that case, the effective band gap energy is given by,

$$E_g{}^* = E_g + (\hbar^2\pi/2\mu r^2) - (1.8e^2/\varepsilon r) + \dots \qquad (2)$$

where r is the particle radius, μ is the effective reduced mass (0.27 m_e for SnO_2), E_g is the bulk band gap energy (3.6 eV), $E_g{}^*$ is the nanoparticle band gap determined from Tauc plot and ε is the dielectric constant (14 for SnO_2). If the size of the nanoparticle is higher than r_B, the 3rd term (Coulomb interaction) in the above equation (2) is considered to be negligible. The particle size ($\bar{a} = 2r$) can be thus calculated. The specific surface area is calculated using the equation (3),

$$S = 6000/(\rho\bar{a}) \qquad (3)$$

where S is the specific surface area, ρ is the density in g/cm^3 and $\bar{a}$ is the particle size in nm.

The carrier concentration was determined to check the effect of B-M shift. The enhanced value of the band gap is given by,

$$E_g = E_g{}^0 + \nabla E_g{}^{BM} \qquad (4)$$

where $E_g{}^0$ is the band gap of the undoped SnO_2 crystal and $\nabla E_g{}^{BM}$ is given by

$$\nabla E_g{}^{BM} = [h^2/2\mu] \times [3\pi^2 n_e]^{2/3} \qquad (5)$$

where h is the Planck's constant, μ is the effective reduced mass and n_e is the carrier concentration. The carrier concentration is deduced using the equation (5).

Photoluminescence spectrum was recorded at room temperature with Jobin Yvon Spectrofluorometer with UV excitation at wavelength, λ = 270 nm.

Results and discussion

Structural and Vibrational Characterization

The XRD pattern shown in Figure 1 confirms the crystallization of tin oxide nanoparticles in single phase without any impurity phase. The tin oxide nanoparticles possess tetragonal rutile crystal structure corresponding to the space group $P4_2/mnm(136)$ and the peaks matches well with the standard JCPDS88-0287.
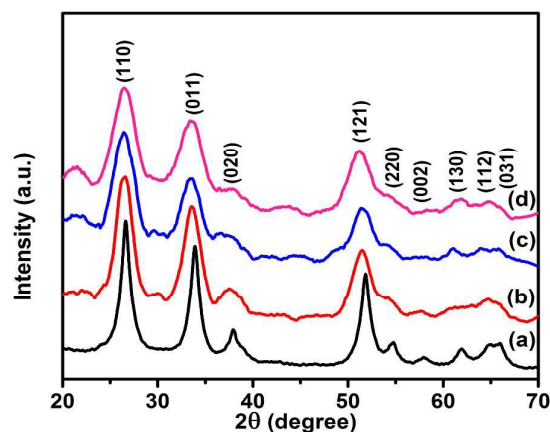

Figure 1 XRD pattern of (a) pristine SnO_2 (b) $Bi_{0.03}Sn_{0.97}O_2$ (c) $Bi_{0.05}Sn_{0.95}O_2$ and (d) $Bi_{0.08}Sn_{0.92}O_2$ ultrananocrystalline particles

ARTICLE

Table 1 Summary of lattice parameters

Sample	Mean Crystallite size *D (nm)	Mean Crystallite size #D (nm)	Mean Crystallite size †D (nm)	Strain ξ	Dislocation density δ (lines/m^2)	Density ρ (g/cm^3)	Lattice constants (Å)	d$_{(110)}$ spacing† (Å)
SnO_2	6.6	6.9	6	0.013	2.24×10^{16}	6.8157	a = 4.78, c = 3.22	3.36
$Bi_{0.03}Sn_{0.97}O_2$	4.3	5.1	4	0.016	5.486×10^{16}	6.7580	a = 4.79, c = 3.23	3.37
$Bi_{0.05}Sn_{0.95}O_2$	3.5	3.8	4	0.018	8.121×10^{16}	6.7023	a = 4.80, c= 3.24	3.37
$Bi_{0.08}Sn_{0.92}O_2$	3.4	3.4	3	0.020	8.252×10^{16}	6.6475	a = 4.81, c = 3.26	3.38

* calculated from Scherrer formula, #calculated from Rietveld structure refinement method, †calculated from SAED

Table 2 Summary of parameters of $Bi_xSn_{1-x}O_2$ (x = 0, 0.03, 0.05, 0.08)

| Sample	Particle size# (ā) nm	Particle size† (ā) nm	Specific surface area S (m^2/g)	Energy band gap (eV)	Carrier Conc. n_e (x10^{19} cm^{-3})
SnO_2	9	9	97.8	3.98	--
$Bi_{0.03}Sn_{0.97}O_2$	7	7	126.8	4.04	3.42
$Bi_{0.05}Sn_{0.95}O_2$	5	5	179.0	4.06	4.09
$Bi_{0.08}Sn_{0.92}O_2$	5	5	180.5	4.07	4.27

#calculated from UV spectral data

†determined by TEM Histogram (See Supporting information S2)

The lattice parameters are summarized in Table 1. According to the 15% rule proposed by Hume,[46] SnO_2 and Bi_2O_3 can easily form a solid solution. There are neither impurity peaks nor peaks related to the dopant observed in the XRD confirming the formation of solid solution. As can be seen from the XRD patterns, the diffraction peaks get broadened as the Bi dopant concentration is increased, suggesting a systematic decrease in the grain size. It can be observed from Table 1 that the crystallite size of SnO_2 nanoparticles reduced from 6 nm to 3 nm as a result of increase in Bi content from 0% to 8%, indicating that the presence of Bi ions in SnO_2 restricted the growth of nanocrystals. The crystallite size of $Bi_{0.08}Sn_{0.92}O_2$ gets reduced to almost half of that of pristine SnO_2 (cf. Table 1). The dopant not only influences the crystal growth but also deteriorates the crystalline nature. It is well-known that the smaller crystallite size tends to reveal the amorphous character. In general, the intensity of the diffraction peaks decreases greatly with the increase of doping concentration, indicating a loss of crystallinity due to lattice distortion. When bismuth ions are incorporated into the periodic crystal lattice

of SnO_2 crystal, defect is formed as well as a strain is induced into the system, resulting in the alteration of the lattice periodicity and decrease in crystal symmetry. The broadening of diffraction planes can be ascribed to the presence of a short range order due to very small crystallites and also due to the presence of non-uniform strain. Lattice strain is also observed to increase with dopant concentration. It is obvious that the lattice strain increases with decrease in crystal size.

A comparison of unit cell volume also reveals that the volume of Bi doped SnO_2 marginally increases with Bi concentration as shown in Figure 2 which can be attributed to the larger ionic radii of Bi as compared to Sn. This indicates lattice expansion due to the incorporation of bismuth ion with large ionic radii into the tin oxide lattice. It can also be interpreted in other way, as the crystallite size decreases it results in increase in unit cell volume marking lattice expansion.

Without any surfactant, ultra-small sized particles have been prepared with high surface area by sonochemical method. The surface area increased from 97.8 m^2/g to 180.5 m^2/g (cf. Table 2) as the Bi content increased from 0% to 8%. There is a linear relationship between surface area and its sensitivity to gas. Therefore, high surface area is advantageous for sensing application.
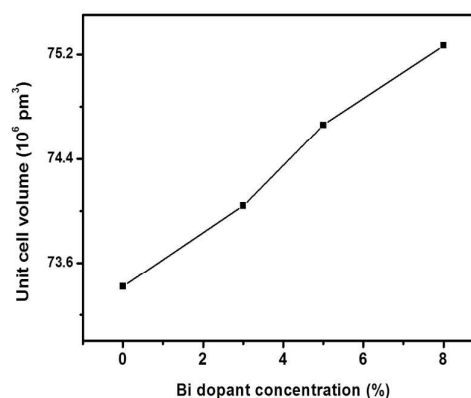
Figure 2 Variation of unit cell volume with Bi dopant concentration in ultrananocrystalline SnO_2
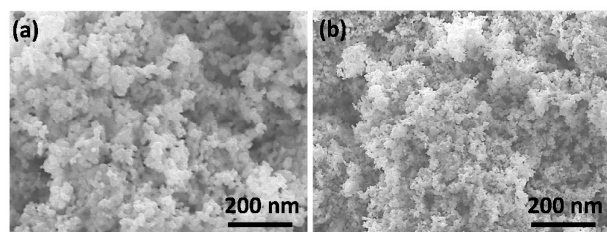
Figure 3 FE-SEM images of (a) pristine SnO_2 ultrananocrystalline particles (b) $Bi_{0.08}Sn_{0.95}O_2$ ultrananocrystalline particles

The surface morphology of the SnO_2 and $Bi_{0.08}Sn_{0.92}O_2$ ultrananocrystalline particles are shown in the Figure 3(a) and (b) respectively, which reveals the presence of equi-axed ultrasmall nanoparticles. The ultrananoparticles have aggregated and formed nanoclusters. The equi-axed crystalline ultrananoparticles assemble into small nanoclusters resembling a broccoli-like structure. High surface area to volume ratio of nanoparticles provides a very high surface energy. To minimize its surface energy the nanoparticles create agglomeration. However, in the present case, it is believed to be soft agglomerates that comprises of a number of ultra-small nanocrystals close to each other. They are neither coalesced nor attached. It is an evident character of ultra-nanocrystalline particles to agglomerate. In order to confirm the ultrananocrystalline nature of the synthesized particles, HRTEM analysis was carried out. Figure 4 shows the bright field TEM image of the series of $Bi_xSn_{1-x}O_2$ ultrananocrystalline particles and their corresponding SAED pattern is shown as insets. The HRTEM image of $Bi_xSn_{1-x}O_2$ shown in Figure 5 confirms the presence of equi-axed ultrananocrystalline particles of diameter ~4-10 nm. The particle size distribution histogram (See Supporting information S2) reveals that the particle size decreases with increase in Bi content. The particle size calculated from UV-Vis spectroscopic data and HRTEM concur very well. The SAED pattern shown as inset reveals the polycrystalline nature of the samples and the ring pattern indicates ultrasmall size of the particles oriented in different direction. Some particles show low contrast which is due to the fact that the electrons are deflected weekly as they are oriented away from the zone axis. The ring pattern corresponds to the (110), (011), (121) and (301) planes respectively. The d-spacing of (110) plane was found to be 3.36Å from the lattice fringes in the HRTEM image.

As Raman scattering is very sensitive to the microstructure of nanocrystalline materials, it is used to confirm the structure of the SnO_2 ultrananocrystals and the effect of substitution of Bi ions on the defect structure. Figure 6 shows the room temperature Raman spectra of the ultrananocrystals of SnO_2 and Bi doped SnO_2. The characteristic Raman active modes, E_g, A_{1g} and B_{2g} are observed at 498 cm^{-1}, 628.5 cm^{-1} and 768 cm^{-1} respectively.[47] Compared to the bulk SnO_2 powder, the observed fundamental vibrational peaks show continuous broadening effect and red shift to the lower wavenumber side with decreasing crystal size corresponding to the increase in Bi content. The shift in the peaks in the observed Raman spectra is associated with the size effect of the ultrananocrystalline

$Bi_xSn_{1-x}O_2$ particles and the probable existence of stress in the utrananocrystallites which leads to the optical phonon confinement.[48] Moreover, the A_{1g} mode softens due to optical phonon confinement effect. Similar softening effect of A_{1g} mode is reported for Silicon.[49] A number of factors are behind the softening of the A_{1g} peak namely reduction in particle size, abundance of structural defects like oxygen vacancies and strain in the lattice due to doping. These fundamental vibrational modes correspond to the tetragonal rutile structure of SnO_2.[48] These fundamental modes of vibration are dominated by new surface vibrational modes which show an enhanced effect upon increasing Bi dopant concentration. This behavior is due to the replacement of Sn ions by Bi ions within the SnO_2 lattice that causes the formation of oxygen vacancy so as to maintain charge neutrality.

In pristine SnO_2, the E_g mode is not obvious whereas appears in doped samples. With increase in Bi dopant concentration, there is marked shift in the E_g mode towards the lower wavenumber side which can be attributed to the reduction in particle size as well as abundance of bridging oxygen vacancies. The size effect and oxygen vancancy induces optical phonon effect as revealed by the peak shift.[48] The peak at 576 cm^{-1} is the unique identification of ultrasmall SnO_2 nanoparticles, as it corresponds to the optically inactive A_{2g} phonon mode by following the Matossi force constant model which considers the modified bond length, space symmetry reduction and lattice distortion due to oxygen vacancies in SnO_2.[51] This strong mode at 576 cm^{-1} can be attributed to the in plane oxygen vacancies. The A_{1g} and A_{2u}(LO) modes can be attributed to bridging oxygen vacancies.[50] The observed B_{2g} mode at 768 cm^{-1} is due the presence of sub-bridging oxygen vacancies in contrast to the 775 cm^{-1} mode corresponding to the structure with no oxygen vacancies.[52]
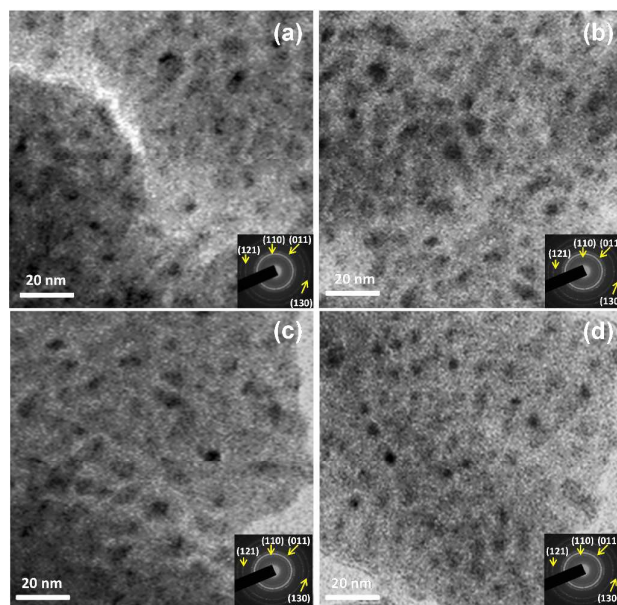

Figure 4 TEM bright field image of (a) pristine SnO_2 (b) $Bi_{0.03}Sn_{0.97}O_2$ (c) $Bi_{0.05}Sn_{0.95}O_2$ and (d) $Bi_{0.08}Sn_{0.92}O_2$ ultrananocrystalline particles and their corresponding SAED pattern shown as insets

ARTICLE
Journal Name
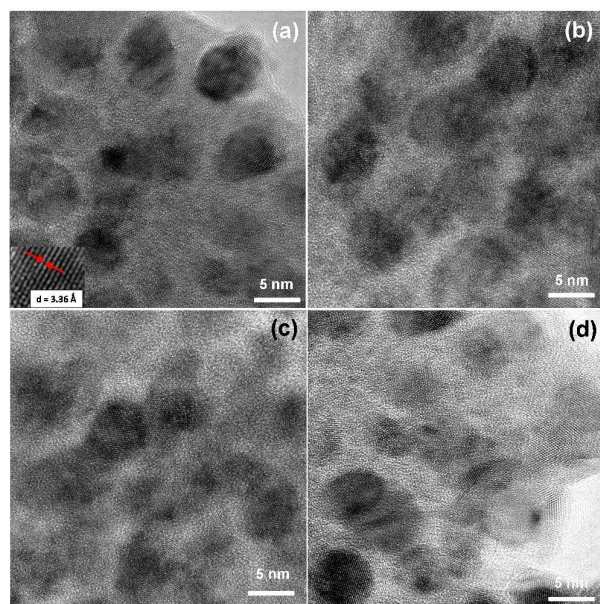

Figure 5 HRTEM image of (a) pristine SnO_2 (b) $Bi_{0.03}Sn_{0.97}O_2$ (c) $Bi_{0.05}Sn_{0.95}O_2$ and (d) $Bi_{0.08}Sn_{0.92}O_2$ ultrananocrystalline particles

Addition of Bi leads to the appearance of the size-related Raman modes. The Raman bands at 245 cm^{-1} - 265 cm^{-1}, 349 cm^{-1} and 603 cm^{-1} are in fact the bands from IR-active E_u modes. The IR active mode transforms into Raman active mode because of the relaxation of the k=0 selection rule induced by the sub-bridging oxygen vacancies. It is interesting to know that the IR active modes, Raman silent mode and optically inactive modes transform to a Raman active mode owing to the size effect and the presence of oxygen vacancies.[53] There is increase in intensity of these bands with increasing bismuth content, which can be correlated to increase in oxygen vacancy due to the incorporated Bi ions inside the SnO_2 lattice. The observed shift in these bands with increasing bismuth content is due to the reduction in grain size and can be attributed to the oxygen vacancy-induced phonon confinement effect. The broadening of Raman peaks signifies the ultrananosize of the particles. D. Bersani et al.[54] also observed peak broadening with decrease in nanocrystallite size.
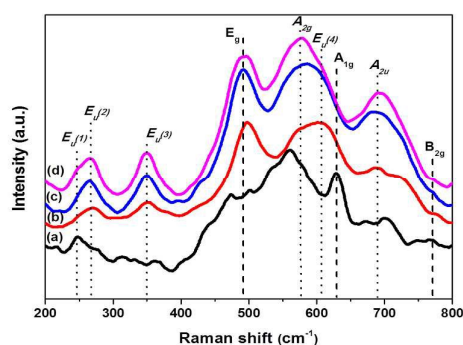

Figure 6 Raman spectra of (a) pristine SnO_2 (b) $Bi_{0.03}Sn_{0.97}O_2$ (c) $Bi_{0.05}Sn_{0.95}O_2$ and (d) $Bi_{0.08}Sn_{0.92}O_2$ ultrananocrystalline particles

The BOLS correlation mechanism could not explain our observed results. The Raman shift observed in the present study is based on Phonon Confinement Model, where the peak shifts to the lower wavenumber side due to phonon confinement by reduction in size, surface stress and structural defects. Loss of stoichiometry due to oxygen deficiency may cause peak broadening effect in Raman spectra.[54] This statement is true in the present case, as the concentration of oxygen vacancy is found to increase with doping and reduced crystallite size, which is evident from O1s XPS spectrum shown in Figure 7. The shift in Raman spectrum can be either due to phonon confinement or as a consequence of shortened apical bond.[55] Strain induced shift in Raman line is also possible.[56] Moreover, the shift and broadening of Raman peak is ascribed to relaxation in the q-vector selection rule for the excitation of Raman active optical phonons. It is further established that the shift in the Raman line increases with decreasing crystallite size.[57]

To support the elucidation of phonon confinement effect by the Raman spectroscopy, XPS O 1s spectrum is obtained for all samples to confirm the presence of oxygen vacancies and is shown as Figure 7. The presence of oxygen vacancies is usually confirmed from the asymmetric broadening effect observed close to ~531 eV in the O1s peak. This profile can be fitted using three symmetrical peaks, namely the low binding energy component (529.5 eV), mid binding energy component (531.2 eV) and high binding energy component (532.3 eV). These three binding energy components are generally assigned to metal oxide bond, oxygen vacancy and surface adsorbed oxygen or hydroxyls respectively.[58] Moreover, it is found that the concentration of oxygen vacancy increases with doping as inferred from increase in asymmetrical broadening of the O 1s spectrum. The survey spectrum is given in Supporting information S3.

Optical and Electronic Properties

Absorption and fluorescence spectroscopy are powerful nondestructive techniques to investigate the optical properties of semiconducting nanoparticles. The optical absorbance measurements were carried out at room temperature and the absorbance spectra of pristine and Bi doped SnO_2 nanoparticles are shown in Figure 8. Absorbance spectra exhibit an absorption peak at around 273 nm which can be attributed to the photo-excitation of electrons from valence band to conduction band. The absorption peak shows a slight blue shift as the concentration of Bi in the SnO_2 nanoparticles increases. It has been observed that the absorbance tends to increase with the increase in dopant concentration. The absorption spectra clearly confirm that both SnO_2 and Bi doped SnO_2 are transparent in visible range.

For semiconductor nanoparticles, the quantum confinement effect is expected. Semiconductor nanoparticles with dimensions in the order of the bulk excition will show unique optical properties, which depend strongly on the size. In semiconductors, band gaps have been found to be particle size dependent. In the present case, the band gap increases with
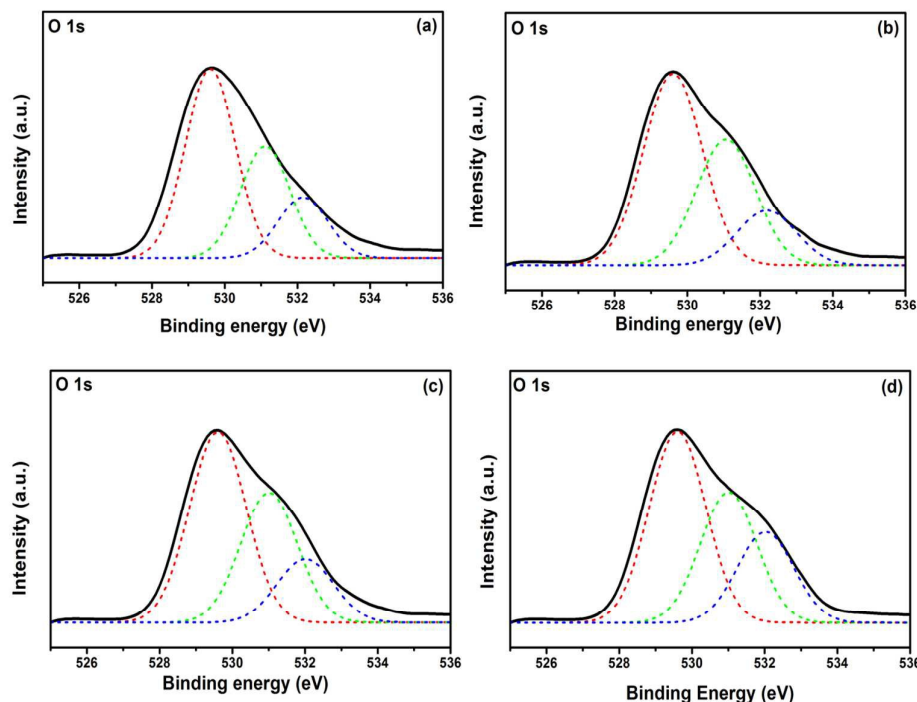
Figure 7 XPS O 1s spectrum of (a) pristine SnO_2 (b) $Bi_{0.03}Sn_{0.97}O_2$ (c) $Bi_{0.05}Sn_{0.95}O_2$ and (d) $Bi_{0.08}Sn_{0.92}O_2$ ultrananocrystalline particles

decreasing particle size indicating that the particles are really in the quantum regime. Figure 9 shows the Tauc plot for determination of electronic energy band gap. The band gap value increases from 3.98 eV to 4.07 eV as the Bi content in the SnO_2 ultrananocrystal increases from 0 to 8% (cf. Table 2). The band gap values reported in the present study is greater than that of the bulk (3.6 eV).[2] This wide band gap can be attributed to the quantum confinement of nanoparticles. Therefore, the change in band gap suggests that the size of the nanoparticles influence the opto-electronic properties of the materials. A slight increase in energy band gap upon incorporation of bismuth dopant is due to BM shift, as a result of the filling of the lower conduction band states in a degenerately doped semiconductor. The carrier concentration (cf. Table 2) is found to increase which causes the BM effect and the increase in band gap energy as the Fermi level moves close to the conduction band. Moreover, the wide band gap and transparency in the visible region combine to make these ultrananocrystalline materials a better choice for opto-electronic applications. Due to ultrafine nanosize of the prepared SnO_2, there are possibilities in exploiting this material as a component for nanoscale light emitters because the dipole-forbidden selection rule may fail due to the breaking of the wave function symmetry in low dimensional systems.[59] As a consequence of the reported wide band gap, it could be of interest for application in photodetectors also. Furthermore, SnO_2 could have a low sensitivity to UV degradation due to its larger band gap and hence may possess better long term stability. SnO_2 is a better electron acceptor since its conduction band edge lies more positive than that of

TiO_2. Therefore, SnO_2-based DSSCs could be attempted to success.

The photoluminescence spectrum was recorded corresponding to an excitation wavelength of 270 nm at room temperature. Upon UV excitation, a diffuse emission peak is observed which can be de-convoluted into three components as shown in Figure 10. The PL emission peaks are centered at 397 - 400 nm, 415 – 416 nm and 439 – 442 nm which correspond to the purple-violet-blue region in the visible spectrum. Bismuth dopant enhances the photoluminescence of the nanomaterial, as inferred by the improvement in the PL intensity.
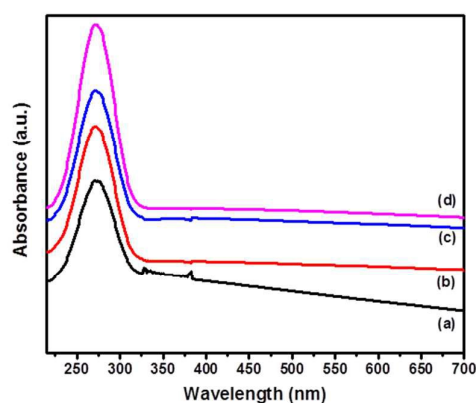

Figure 8 UV-Visible absorption spectra of (a) pristine SnO_2 (b) $Bi_{0.03}Sn_{0.97}O_2$ (c) $Bi_{0.05}Sn_{0.95}O_2$ and (d) $Bi_{0.08}Sn_{0.92}O_2$ ultrananocrystalline particles

Journal Name

ARTICLE
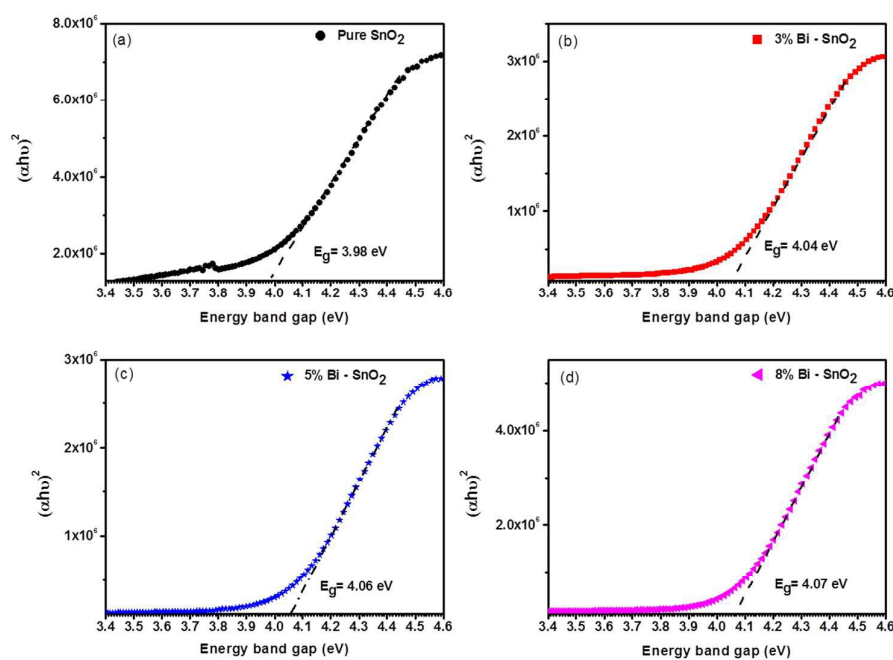
Figure 9 Tauc plots of (a) pristine SnO_2 (b) $Bi_{0.03}Sn_{0.97}O_2$ (c) $Bi_{0.05}Sn_{0.95}O_2$ and (d) $Bi_{0.08}Sn_{0.92}O_2$ ultrananocrystalline particles

An increase in PL intensity in the luminescence spectra can occur due to increase in both the surface to volume ratio and concentration of oxygen vacancies. The observed PL intensity enhancement is in good agreement with the decreasing trend in grain size as determined by XRD analysis and the increase in oxygen vacancy concentration as observed in Raman spectra and XPS. As the emission maximums observed at 3.1 eV, 2.98 eV and 2.8 eV are lower than the band gap of the SnO_2 nanocrystal (~4 eV), the visible emission cannot be assigned to the direct recombination of an electron in the Sn 4p conduction band and a hole in the O 2p valance band. The photoluminescence in tin oxide nanoparticles is associated with defect energy levels that lie within the band gap. The most common defects present in oxides are oxygen vacancies, which generally acts as radiative centre in the luminescence processes. Thus, the nature of the transition can be tentatively ascribed to oxygen vacancies, Sn vacancies or Sn interstitials, which act as trap states within the band gap. The peak maximum at ~415 nm might originate from the luminescence centers formed by such tin interstitials or dangling present in the SnO_2 nanoparticles. The emission at ~400 nm can be attributed to the electron transition mediated by defect levels in the band gap such as oxygen vacancies. In the present SnO_2 nanocrystals, the intrinsic defects, such as oxygen vacancies, which act as luminescent centers, can form defect levels located highly in the gap, trapping electrons from the valence band to make a contribution to the luminescence. Generally, in poly- and nano-crystalline oxides, oxygen vacancies are known to be the most common defects and usually act as radiative centers in luminescence processes. Also, the oxygen vacancies can be present in three different charge states: V_o^0, V_o^+, and V_o^{++}. The oxygen vacancy is an intrinsic donor in SnO_2. The blue emission corresponding to the strong shoulder at ~441 is due to the in-plane oxygen vacancies induced defect electronic states.[60, 61] The radiative process for blue emission band is V_o^{++} + e'_{CB} → V_o^+ + hv_o; the recombination of the deeply trapped charges and photo-generated electrons from the conduction band.[62]

As the Bi content increases, the particle size of the SnO_2 nanocrystal becomes smaller and the oxygen vacancies-related luminescence intensity increases remarkably. This can be attributed to the significant increase of both the surface defects and concentration of oxygen vacancies of the SnO_2 nanoparticles. Therefore, the rate for a surface trapping process increases as the particle size decreases since the surface to- volume ratio increases. Upon incorporation of Bi ions in the host lattice, the charge neutrality is maintained by the formation of oxygen vacancy. With increasing content of Bi

Journal Name

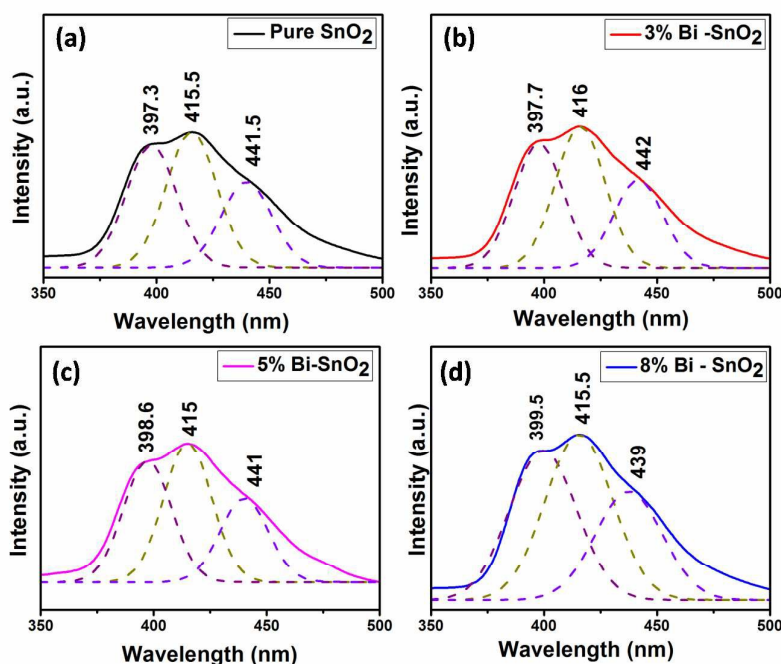## ARTICLE

Figure 10 Room temperature photoluminescence spectra of (a) pristine SnO_2 (b) $Bi_{0.03}Sn_{0.97}O_2$ (c) $Bi_{0.05}Sn_{0.95}O_2$ and (d) $Bi_{0.08}Sn_{0.92}O_2$ ultrananocrystalline particles

ions, more V_o^+ centers are formed. As a consequence, in such a situation there is a chance for more holes to get trapped by these V_o^+ centers to form V_o^{++} recombination centers upon photoexcitation of the SnO_2 nanoparticles. Hence, the intensity of emission in luminescence is enhanced in Bi doped samples.

Tin dioxide is a multifunctional semiconductor with excellent electrical and optical properties. So as to the performance in existing applications and enable new ventures, such as in light emitters a better understanding of the emission is important. The investigated SnO_2 can be a promising material for photonic applications in the violet blue spectral range.[60, 61] SnO_2 has unique properties that makes it advantageous over other wide band gap semiconductors, such as GaN and ZnO, and therefore can be used for fabricating short wavelength optoelectronic devices. In summary, SnO_2 holds great promise for a variety of optoelectronic applications and has very interesting and varied materials properties. To materialize the inexpensive, stable, environment-friendly and high efficient light emitting and photo-detection devices, better control and understanding of the properties of SnO_2 material is necessary, which is expected to result in controllable and reproducible achievement of desired properties and device performance.

Conclusions

In summary, pristine SnO_2 and Bi-doped SnO_2 ultrananoparticles were successfully synthesized using sonochemical method. The XRD spectra confirm the tetragonal rutile structure of all the samples and moreover, no impurity phase was observed in XRD. It was found that with the increase in bismuth concentration there was a decrease in the crystallanity and crystallite size. The unit cell volume increases with the incorporation of large ionic radii dopant Bi into the host lattice and the reduction in crystallite size indicating the phenomena of lattice expansion. The three fundamental Raman modes of SnO_2 ultrananoparticles also confirm the rutile symmetry of all the samples. Optical band gap was found to vary from 3.98 eV to 4.07 eV with doping due to BM shift. The ultrananocrystalline nature, wide band gap and transparency in visible region enable SnO_2 to be a transparent conducting oxide which finds application as transparent electrodes, surface coatings and solar cells. The concentration of oxygen vacancy increases with increasing Sn ion replacement with Bi ions marked by the peak shift and peak broadening of the Raman line as well as intensity enhancement of emission peak in photoluminescence. The

ARTICLE

presence of oxygen vacancy is further confirmed from the asymmetrical broadening of O 1s XPS profile. Finally, structural and optical studies conclude that the Bi ions are successfully incorporated into the lattice position of Sn ion in SnO_2 crystal lattice and the process may be used to optimize the band gap and particle size and hence the material may be used in opto-electronic devices. Optical phonon confinement effect is observed in the ultrananocrystalline $Bi_xSn_{1-x}O_2$ system as confirmed from Raman spectroscopic analysis. Interestingly, the IR active modes, Raman silent mode and optically inactive modes transform to a Raman active mode owing to the size effect and the presence of oxygen vacancies. The ultrananocrystal with more Bi content is found to be rich in oxygen vacancies. The defect structure comprises of the in-plane, bridging and sub-bridging oxygen vacancy in the ultrananocrystalline $Bi_xSn_{1-x}O_2$ system.

Acknowledgements

References

1 S. H. Lee, D. M. Hoffman, A. J. Jacobson and T. R. Lee, *Chem. Mater.*, 2013, **25 (23)**, 4697–4702.
2 B. Nandan, B. Venugopal, S. Amirthapandian, B. K. Panigrahi and P. Thangadurai, *J. Nanopart. Res.*, 2013, **15**, 1999.
3 L. Man, J. Zhang, J. Wang, H. Xu and B. Cao, *Particuology*, 2013, **11**, 242.
4 P.T. Wierzchowski, L.W. Zatorski, *Appl. Catal. B: Environ*, 2003, **1352**, 1–13.
5 T.E. Moustafid, H. Cachet, B. Tribollet and D. Festy, *Electrochim. Acta*, 2002, **47(8)**, 1209–1215.
6 A. Birkel, Y. -G. Lee, D. Koll, X. V. Meerbeek, S. Frank, M. J. Choi, Y. S. Kang, K. Char and W. Tremel, *Energy Environ. Sci.*, 2012, **5**, 5392-5400.
7 L. Mei, Y. Chen and J. Ma, *Sci. Rep.,* 2014, 4, 6028.
8 Y. -G. Kang, H. -J. Kim, H. -G. Park, B. -Y. Kim and D. -S. Seo, *J. Mater. Chem.*, 2012, **22**, 15969-15975.
9 W. Tian, C. Zhang, T. Zhai, S. -L. Li, X. Wang, M. Liao, K. Tsukagoshi, D. Golberg and Y. Bando, *Chem. Commun.*, 2013, **49**, 3739-3741.
10 H. -C. Chu, Y. -S. Shen, C. -H. Hsieh, J. -H. Huang and Y. -H. Wu, *ACS Appl. Mater. Interfaces*, 2015, 7(28), 15129–15137.
11 X. Zhou, Y. -X. Yin, L. -J. Wan and Y. -G. Guo, *J. Mater. Chem.*, 2012, **22**, 17456-17459.
12 W. Li, C. Shen, G. Wu, Y. Ma, Z. Gao, X. Xia and G. Du, *J. Phys. Chem. C*, 2011, **115 (43)**, 21258–21263.
13 G. -J. Li, S. Kawi, *Mater. Lett.*, 1998, **34(1–2)**, 99–102.
14 S. Chaisitsak, *Sensors*, 2011, **11(7)**, 7127-7140.
15 K Suematsu, Y. Shin, Z. Hua, K. Yoshida, M. Yuasa, T. Kida and K. Shimanoe, *ACS Appl. Mater. Interfaces*, 2014, **6 (7)**, 5319–5326.
16 A. Sharma, M. Tomar and V. Gupta, *Sens. Actuators, B*, 2013, **181**, 735–742.
17 L. Wang, Y. Chen, J. Ma, L. Chen, Z. Xu and T. Wang, *Sci. Rep.*, 2013, **3**, 3500.
18 L. P. Chikhale, J. Y. Patil, F. I. Shaikh, A. V. Rajgure, R. C. Pawar, I. S. Mulla and S. S. Suryavanshi, *Mater. Sci. Semicond. Process.*, 2014, **27**, 121–129.

19 G. Zhang, M. Liu, *Sens. Actuators. B. Chem.*, 2000, **69**, 144.
20 J. M. Xu, L. Li, S. Wang, H. L. Ding, Y. X. Zhang and G. H. Li, *CrystEngComm*, 2013, **15**, 3296
21 H. Jin, Y. Xu, G. Pang, W. Dong, Q. Wan, Y. Sun and S. Feng, *Mater. Chem. Phys.*, 2004, **85**, 58.
22 J. Hays, A. Punnoose, R. Baldner, M.H. Engelhard, J. Peloquin and K.M. Reddy, *Phys.Rev. B*, 2005, **72**, 075203.
23 G. Korotcenkov, V. Macsanov, V. Brinzari, V. Tolstoy, J. Schwank, A. Cornet and J.Morante, *Thin Solid Films*, 2004, **467**, 209.
24 A. Azam, A. S. Ahmed, M. S. Ansari, M. M. Shafeeq and A.H. Naqvi, *J. Alloys Compd.*, 2010, **506**, 237.
25 F. Gu, S. F. Wang, M. K. Lu1, G. J. Zhou, D. Xu and D. R. Yuan, *J. Phys. Chem. B.,* 2004, ***108***, 8119-8123
26 W. Donga, X. Xiea, J. Jiaa, H. Dua, L. Zhonga, Z. Lianga and P. Han, *Electrochim. Acta.*, 2014, **132**, 307–314
27 H. Liu, A.Vajpayee, and C. D. Vecitis, *ACS Appl. Mater. Interfaces.*, 2013, **5**, 10054–10066.
28 A. Henglein, *Chem. Rev.*, 1989, **89**, 1861.
29 D. Manoharan, L. Aswaghosh and N. V. Jaya, *Int.J. ChemTech Res.,* 2014, **7**, 1634–1638. W. Shi, Y. F. Zheng, N. Wang, C. S. Lee and S. T. Lee, *Appl. Phys. Lett.,* 2001, **78**, 3304.
30 W. Shi, Y. F. Zheng, N. Wang, C. S. Lee and S. T. Lee, *Appl. Phys. Lett.,* 2001, **78,** 3304.
31 G. Turrell, *Infrared and Raman Spectra of Crystals*, Academic, London, 1972.
32 D. A. Long, *Raman Spectroscopy,* McGraw Hill, New York, 1977.
33 V. K. Malinovsky, A. P. Sokolov, *Solid State Commun.* 1986, **57**, 757.
34 A. K. Arora, D. U. Bartholomew, D. L. Peterson and A. K. Ramdas, *Phys. Rev., B,* 1987, **35**, 7966.
35 P. Verma, L. Gupta, S. C. Abbi and K. P. Jain, *J. Appl. Phys.* 2000, **88**, 4109
36 F.D. Demangeot, V. Paillard, P. M. Chassaing, C. Pages, M.L. Kahn, A. Maisonnat and B. Chaudret, *Appl. Phys. Lett.* 2006, **88**, 071921.
37 A. Pottier, S. Cassaignon, C. Chaneac, F. Villain, E. Tronc and J. P. Jolivet, *J. Mater. Chem.,* 2003, **13**, 877.
38 F. Li, L. Chen, Z. Chen, J. Xu, J. Zhu and X. Xin, *Mater. Chem. Phys.*, 2002, **73**, 335–338.
39 H. -Y. Wang, G. -Y. Liu, Z. -Z. Yang, B. -Y. Wang, L. Chen and Q. -C. Jiang, *Int. J. Electrochem. Sci.*, 2013, **8**, 2345 – 2353
40 Y. C. Goswami, V. Kumar, P. Rajaram, V. Ganesan, M. A. Mali k and P. O'Brien**,** *J. Sol-Gel Sci. Technol.*, 2014, 69(3), 617-624.
41 L. C. Nehru, C. Sanjeeviraja, *J. Adv. Ceram*, 2014, 3(3), 171-176
42 S. K. Tripathy , A. Mishra, S. K.   Jha, R. Wahab   and A. A. Al-Khedhairy, *J. Mater. Sci. - Mater. Electron.*, 2013, 24(6), 2082-2090
43 C. A. Ibarguen, A. Mosquera, R. Parra, M. S. Castro and J.E. R. Páez, *Mater. Chem. Phys.,* 2007, **101,** 433.
44 D. Manoharan, L. Aswaghosh, K. Vishista and N. V. Jaya, *Ultrason. Sonochem*., 2015, **23**, 174–184.
45 A. L. Patterson, *Phys. Rev.*, 1939, **56**, 978–982.
46 W. H. Rothery, in *Phase stability in metals and alloys*, ed. P.S.Rudman, J.Stringer and R.I. Jaffee, McGraw Hill, New York, 1967, pp 3-23.
47 J. F. Scott, *J. Chem. Phys.*, 1970, **53**, 852.
48 I. H. Campell, P. M. Fauchet, *Solid State Commun.*, 1986, **58**, 73
49 S.K. Gautam, F. Singh, I. Sulania, R. G. Singh, P.K. Kulriya and E. Pippel, *J. Appl. Phys.*, 2014, **115**, 143504
50 L. Z. Liu, T. H. Li, X. L. Wu, J. C. Shen and P. K. Chu, *J. Raman Spectrosc.*, 2012, **43**, 1423-1426
51 F. Matossi, *J. Chem. Phys.*, 1951, **19**, 1543.

52 L.Z. Liu, X.L. Wu, T.H. Li and J. C. Shen, *Appl. Surf. Sci.*, 2015, **347,** 265-268.

53 T.H. Li, L.Z. Liu, X.X. Li, X. L. Liu, H.T. Chen, P.K. Chu, *Opt. Lett.*, 2011, **36 (21)**, 4296-4298.

54 D. Bersani, P.P. Lottice and X.-Z Ding, *Appl. Phys. Lett.*, 1998, **72**, 73 - 75.

55 C.R. Aita, *Appl. Phys. Lett.*, 2007, **90**, 213112.

56 X.X. Yang, J. W. Li, Z. F. Zhou, Y. Wang, L.W. Yang, W.T. Zheng and C. Q. Sun, *Nanoscale.*,2012, **4**, 502-510

57 H. Richter, Z. P. Wang and L. Ley, *Solid State Commun.*, 1981, **39**, 625-629.

58 S. Shi, D. Gao, Q. Xu, Z. Yang and D. Xue, *RSC Adv*, 2014, **4**, 45467-454672

59 W. Zhou, R. Liu, Q. Wan, Q. Zhang, A. L. Pan, L. Guo, B. Zou, *J. Phys. Chem. C.*, 2009, **113,** 1719-26.

60 B. VenkataRamana, A. Das, A.K. Prasad, N. Gopala Krishna, S. Dhara and A.K. Tyagi, *Appl. Phys. Lett.*, 2014, **105**, 243102.

61 B. Venkataramana, A. Das, S. Amirthapandian, S. Dhara and A.K. Tyagi, *Phys. Chem. Chem Phys*., 2015, **17**, 9794.

62 F. Gu, S. F. Wang, M. K. Lu1, G. J. Zhou, D. Xu and D. R. Yuan, *J. Phys. Chem. B.*, 2004, **108**, 8119-8123